

# Multi-technique damage monitoring of concrete beams: Acoustic Emission, Digital Image Correlation, Dynamic Identification

Giuseppe Lacidogna, Gianfranco Piana, Federico Accornero\*, Alberto Carpinteri

Department of Structural, Geotechnical and Building Engineering, Politecnico di Torino, Corso Duca degli Abruzzi 24, 10129 Torino, Italy

## HIGHLIGHTS

- Damage monitoring and analysis take advantage of a multi-technique approach.
- Scaling laws are obtained for fracture energy, bending strength, and AE energy.
- The strain state obtained by DIC is put in relation with the crack path.
- An estimate of the crack advancement is obtained by resonant frequency analysis.

## ARTICLE INFO

### Article history:

Received 9 July 2019

Received in revised form 27 December 2019

Accepted 5 January 2020

### Keywords:

Pre-notched concrete beam

Crack propagation

Acoustic Emission

Digital Image Correlation

Dynamic Identification

Size-scale effect

Fractal domain

Fractal parameter

## ABSTRACT

Acoustic Emission (AE), Digital Image Correlation (DIC) and Dynamic Identification (DI) techniques are used to analyse crack formation and propagation in plain concrete pre-notched beam specimens subject to three-point bending. Four dimensional scales are considered and scale effects on fracture energy, bending strength, and AE energy per unit area are investigated. The energy brittleness numbers are calculated for the different beam sizes to characterise the fragility of the specimens. For the larger sample, the principal strain directions obtained by DIC are put in relation with the crack path, while the analysis of resonant frequencies is used to correlate the bending stiffness reduction to the crack advancement.

© 2020 Elsevier Ltd. All rights reserved.

## 1. Introduction

As is well-known, failure of pre-notched plain concrete beams under bending is basically governed by the tensile strength or the fracture toughness, depending on the geometrical scale (beam size), and the value of the relative notch depth. Schematically speaking, the former case is typical of relatively small beams made of low-strength concrete and with a large relative notch depth, and is characterised by a relatively ductile structural behaviour (stable crack propagation); the latter case, typical of relatively large beams made of high-strength concrete and with a small relative notch depth, is characterised by a brittle structural behaviour (unstable crack propagation) [1].

In the present study, three-point bending (TPB) tests were performed on plain concrete pre-notched specimens of four different sizes to investigate the damage process that takes place when the dimensional scale is increased, while maintaining all the remaining parameters unchanged. Reference was done to RILEM Recommendations [2,3] as regards the testing procedure and the evaluation of Fracture Energy and bending strength. In order to take advantage of interdisciplinary research [4], three non-destructive monitoring techniques such as Acoustic Emission (AE), 2D Digital Image Correlation (DIC) and Dynamic Identification (DI), were adopted during the tests, thus allowing to collect independent information coming from the different techniques.

The former technique is based on the acquisition of ultrasonic signals generated by crack formation and propagation in the material bulk: interesting results can be obtained for, among others, concrete and masonry structures (e.g., see [5,6]). Beside the evaluation of damage indicators, analysis of AE signals also allows for investigating microcracking and damage from an energy

\* Corresponding author.

E-mail addresses: [giuseppe.lacidogna@polito.it](mailto:giuseppe.lacidogna@polito.it) (G. Lacidogna), [gianfranco.piana@polito.it](mailto:gianfranco.piana@polito.it) (G. Piana), [federico.accornero@polito.it](mailto:federico.accornero@polito.it) (F. Accornero), [alberto.carpinteri@polito.it](mailto:alberto.carpinteri@polito.it) (A. Carpinteri).

viewpoint [7–10]. In this study, scale effects on fracture energy, bending strength, and AE energy per unit area were investigated. In particular, the fractal dimensions of the domains associated to fracture and AE energy detected during TPB tests were calculated and compared in order to highlight the difference between dissipated and emitted energy.

On the other hand, DIC is a powerful non-contact optical technique for measuring displacement and strain based on accurate 2D and 3D tracking and registration of changes in images [11,12]. Recently, Shrama et al. combined AE and DIC measurements for damage characterization of welded joints [13], full field strain pattern from DIC were successfully correlated with AE indices in masonry by Livitanos et al. [14], and numerical simulations were also performed for validation and prediction purposes. Moreover, a detailed experimental investigation of fracture process using DIC in plain and reinforced concrete beams under bending can be found in [15].

It is also known as non-destructive dynamic testing of structures, based on well-developed DI techniques, can be used to obtain information about damage level and location. In this case, variations in modal parameters as frequencies and curvatures can be associated to location and depth of cracks [16–24]. This latter technique was also adopted in this study to estimating the crack depth by comparing the resonant frequencies measured during the loading (and damage) process with those of FEM models of similar specimens with different notch depths.

In previous studies [23,24], some of the authors have investigated the damage progress in plain concrete specimens under bending by combining AE and DI techniques. In the present study, DI, AE, and DIC were applied simultaneously. Indeed, global information on the structural stiffness can be gathered by analysing the variation of the resonant frequencies with the cracking progress, whereas local information on a critical region can be collected from the other two techniques. Basically, DIC allows to reconstruct the surface strain state within the monitored area; those strains can be used to get an estimate of the stress state, by adopting a selected constitutive law, as well as to investigate on the principal strain/stress directions. Such information are useful for predicting the formation of new cracks or detecting advancement of existing ones, as well as for tracking the crack path. On the other hand, AE signal analysis allows to classify the cracking mode, and, with a sufficient number of sensors, localise points where microcracking originates.

In principle, the multi-technique approach applied here to laboratory tests on small-size specimens can be extended to real world structures to realise a more effective and reliable monitoring. Investigation may proceed vertically, from general to local, as well as horizontally, by crossing the information from the different techniques. For example, modal frequencies, shapes and curvatures can be used to detect anomalies in the dynamic behaviour of a structure with respect to the undamaged state, and to detect the possible damaged regions. Thus, AE sensors and DIC apparatus can be placed around those specific regions and the relevant data, together with the dynamic parameters, used for monitoring the structural health or damage evolution process.

## 2. Materials and methods

Specimens with rectangular cross-section and a relative notch depth ( $a/b$ ) equal to 0.5 were considered. Geometrical dimensions prescribed by [2,3] were adopted for three-point bending testing (Table 1). Tests were conducted in displacement-controlled mode by servo-hydraulic universal testing machines. Smaller beams, with depth = 100 mm, were tested on a MTS with a maximum loading capacity of 100 kN. For convenience in terms of

**Table 1**  
Specimen sizes considered in the experimental campaign according to [2,3].

Depth $b$ (mm)	Width $t$ (mm)	Length $L$ (mm)
100 ± 5	100 ± 5	840 ± 10
200 ± 5	100 ± 5	1190 ± 10
300 ± 5	150 ± 5	1450 ± 10
400 ± 5	200 ± 5	1640 ± 10

experimental set-up, beams of larger sizes were tested on a Baldwin machine with maximum loading capacity of 500 kN (Fig. 1). Three tests were conducted on specimens with  $b = 100$  mm; two tests on beams with  $b = 200$  mm; one test on a beam with  $b = 300$  mm; and three tests on beams with  $b = 400$  mm. The mechanical properties of the concrete constituting the beams are the following: mass density  $\rho = 2310$  kg/m<sup>3</sup>; cubic compression strength  $R_c = 26.4$  MPa; cylindrical compression strength  $f_c = 21.9$  MPa; average tensile strength  $f_{ct} = 2.4$  MPa; average elastic modulus  $E_c = 30,570$  MPa.

All the samples tests up to final collapse. During TPB tests, AE events emerging from damage of specimens were detected by resonant piezoelectric transducers (resonant frequency = 160 kHz) by Leane Net S.r.l. (Sarzana, Italy), stuck on the specimen's surface near the notch by a silicon glue (Fig. 1c). Waveforms were recorded by setting the sampling frequency to 1 Msample/s and the acquisition threshold level to 2 mV. The data were collected by a National Instruments digitizer capable up to 8 channels. The AE waves, captured by the sensors, were pre-amplified with 60 dB gain before signal processing.

At the same time, DIC measurements were performed on specimens with  $b = 400$  mm, by means of VIC-2D system by Correlated Solutions. Fig. 1a shows the set-up of a test with the DIC apparatus, whereas Fig. 1b shows a detail around the mid-span section, cracked after final collapse. Furthermore, a beam with  $b = 400$  mm was equipped with four JPR Plustone 400–403 piezoelectric pickups for the extraction of resonant bending frequencies (see [25]) in correspondence to different loading levels (Fig. 1c). The pickups, operating in the frequency range ~0–20 kHz, were coupled to an 8-channel Audiombox 1818VS1 acquisition device by PreSonus (Baton Rouge, LA, USA). Free vibration response signals induced by impact excitation were acquired by setting the sampling frequency to 48 kHz. A combined use of AE and DI techniques for damage monitoring of pre-notched plain concrete specimens of smaller size ( $b = 100$  mm), tested under three- and four-point bending, can be found in [23,24].

## 3. Results

The fractal model of the damaged microstructure in quasi-brittle and disordered materials allows defining scale-invariant material properties [26–29]. According to that model, it is known that: for tensile (bending) strength, the fractal dimension of material ligament at peak stress is  $\Delta_\sigma < 2$  (lacunar domain); for fracture energy, the fractal dimension of fracture surface at failure is  $\Delta_C > 2$  (invasive domain). An interesting result is obtained here for AE energy per unit area: as it will be shown in this section, data show that it is emitted on a lacunar fractal domain ( $\Delta_{AE} < 2$ ).

Fig. 2a shows the load–deflection curves obtained by the TPB tests. Different families corresponding to the different specimen sizes can be distinguished: the dispersion of the curves corresponding to the same family is due to the statistical distribution of material properties and heterogeneity of concrete in different specimens. Also, the different trends of the post-peak branches (i.e., the steepness of the negative slope of the softening branch and the maximum deflection-to-maximum force ratio)

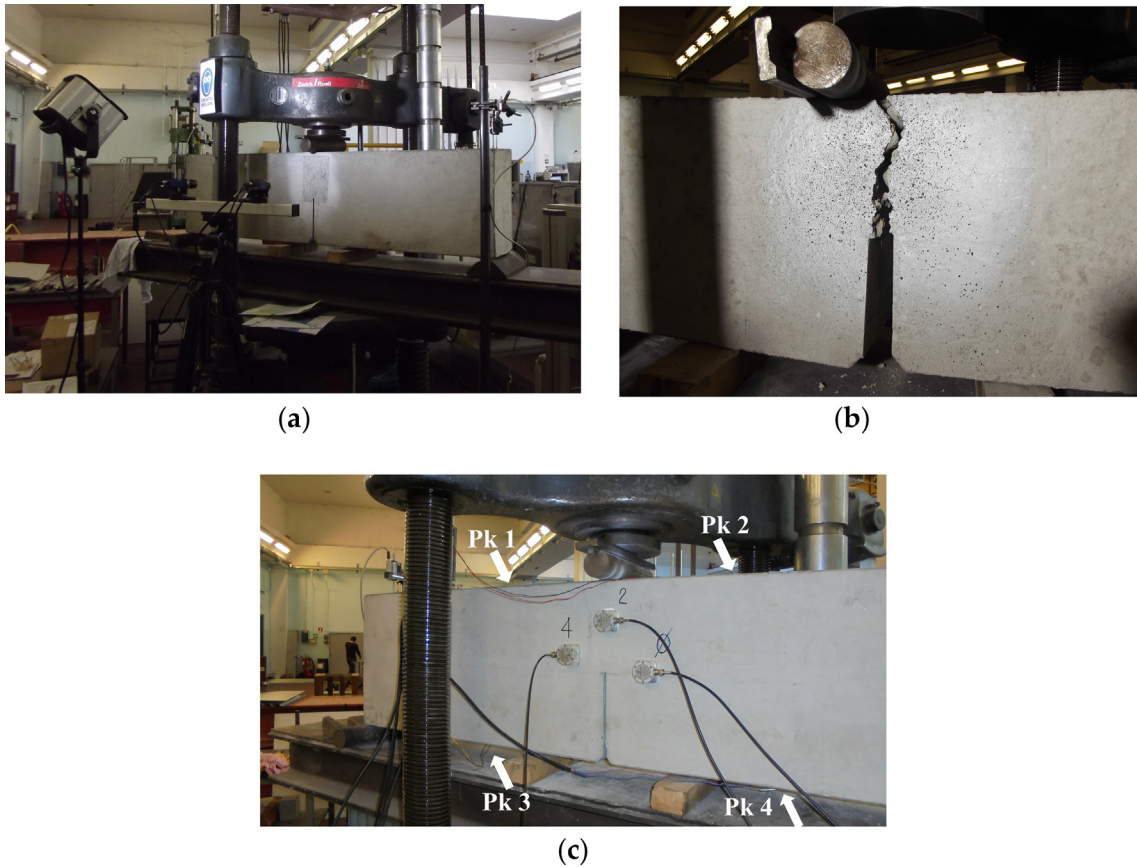


Fig. 1. Beam specimen with  $b = 400$  mm: (a) experimental set-up for DIC measurements; (b) mid-span region after collapse; (c) instrumentation with three AE sensors, and four pick-ups (Pk 1-Pk 4) for extraction of resonant frequencies.

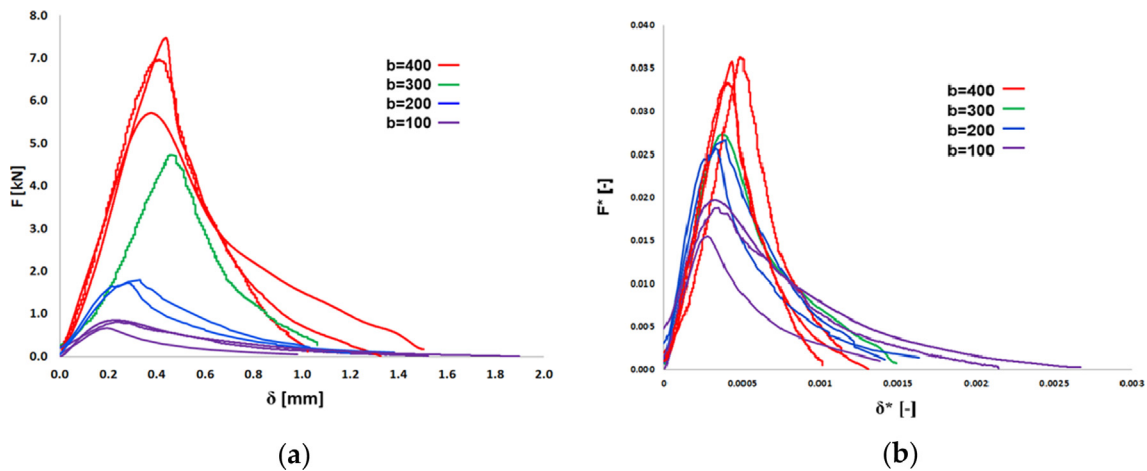


Fig. 2. (a) Load-deflection curves, and (b) renormalized load-deflection curves from TPB tests.

corresponding to the different specimen sizes are due both to scale effect and different mix-design of concrete according to [2,3]: smaller specimens exhibit a more ductile post-peak behaviour while larger specimens show a more brittle one. By introducing a proper renormalization of load and deflection values, a decrease in dispersion can be obtained; i.e., we tend toward a description of the post-peak mechanical response of the specimens that is independent of the scale (the softening branches coalesce in the theoretical case). For this purpose, the renormalized bending

strength,  $\sigma_u^*$ , and the rescaled dimension of the ligament are used. Thus, the dimensionless value of the load turns into [29]:

$$F^* = \frac{F}{\sigma_u^* t b^{1-d_\sigma}} \quad (1)$$

where  $d_\sigma$  is the corresponding fractal exponent.

In a similar way, the dimensionless value of the deflection can be evaluated as:

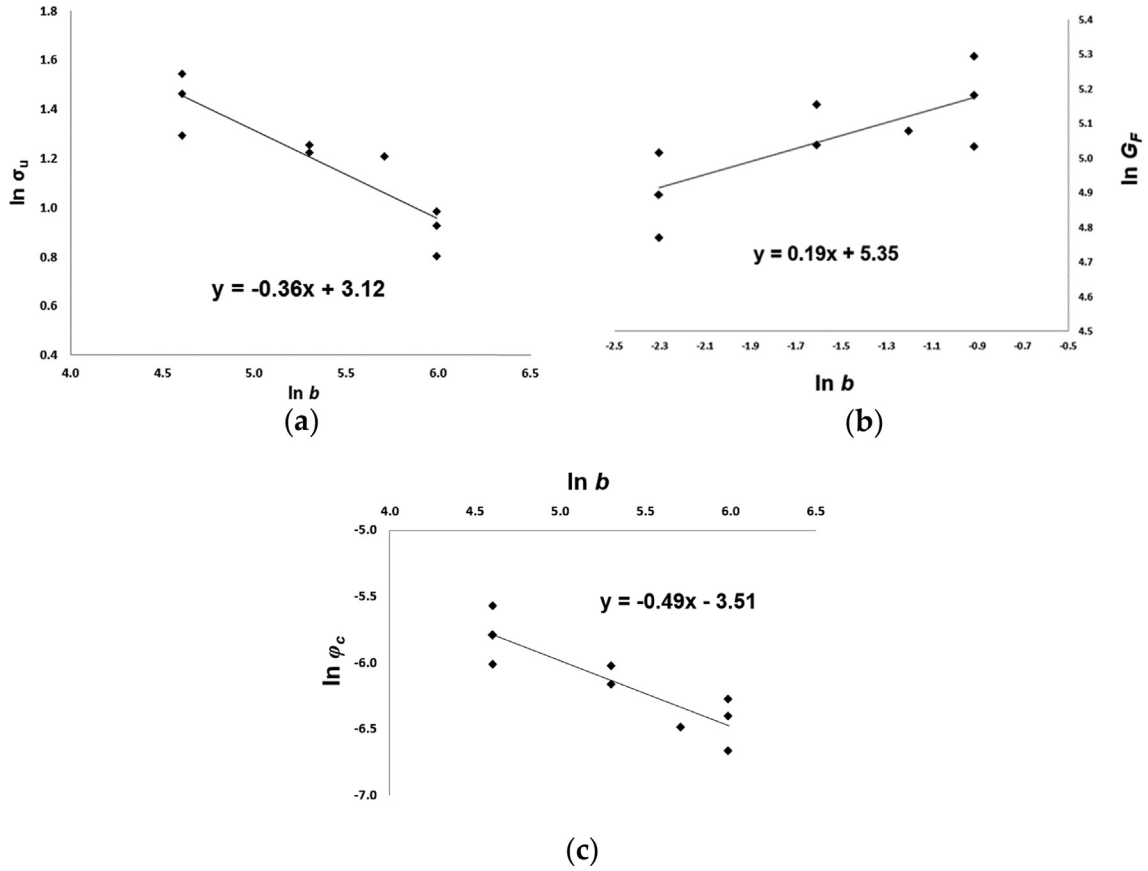


Fig. 3. (a) Bending strength, (b) fracture energy, and (c) critical rotation vs. beam depth.

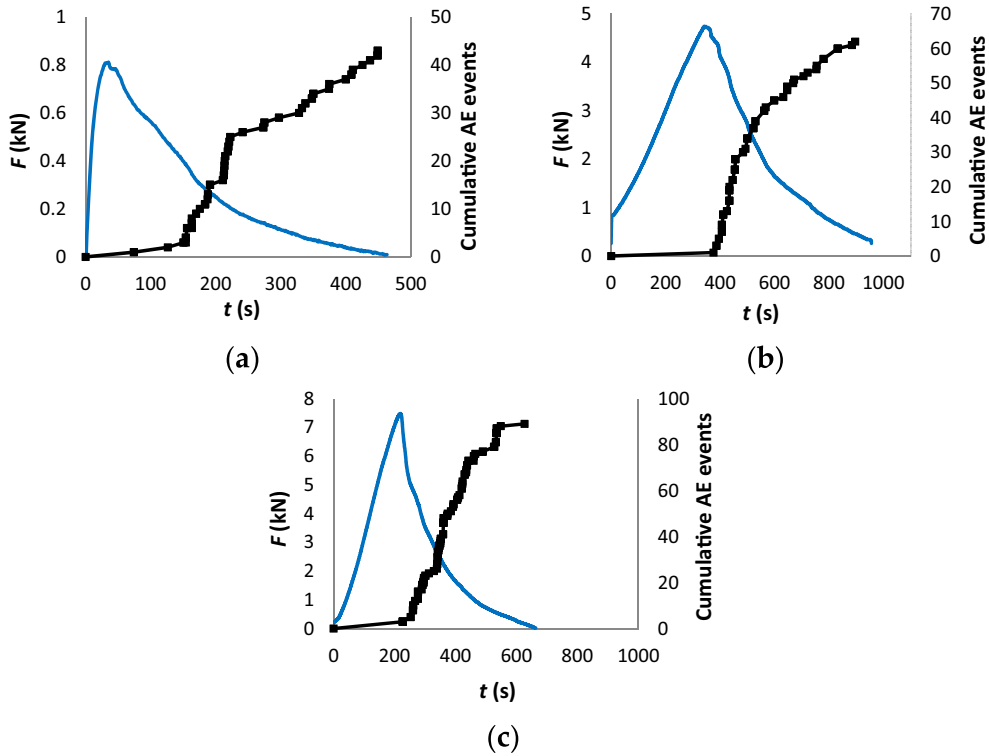


Fig. 4. Loading history (black line) and cumulative AE events (blue line) vs. time for (a)  $b = 100$  mm, (b)  $b = 300$  mm, (c)  $b = 400$  mm. (For interpretation of the references to colour in this figure legend, the reader is referred to the web version of this article.)

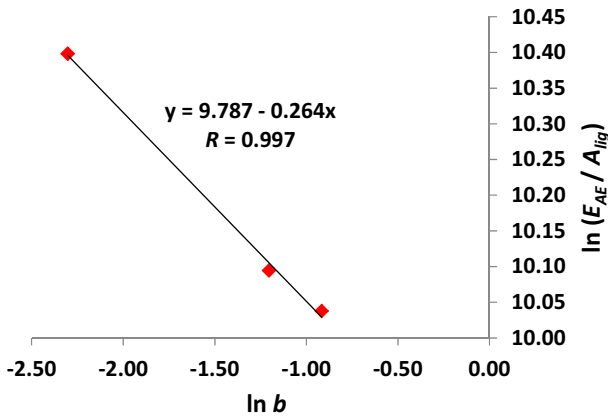


Fig. 5. AE energy per unit area vs. beam depth ( $R$  is the Pearson correlation coefficient).

$$\delta^* = \frac{\delta \chi_c^*}{b^{1-d_\chi}} \quad (2)$$

where  $\chi_c^*$  is the renormalized critical curvature, and  $d_\chi$  is the corresponding fractal exponent [29]. The load-deflection curves renormalized according to Eqs. (1) and (2) are shown in Fig. 2b. The values of the renormalized and fractal parameters involved will be defined hereafter.

In Fig. 3a, the bending strength vs. specimen size (beam depth) values are reported in a bi-logarithmic diagram. The bending strength  $\sigma_u$  is computed assuming a linear stress distribution along the ligament ( $\sigma_u = M_{max}/W_{lig} = 6FL/tb^2$ ). The relevant fractal scaling law reads:

$$\ln \sigma_u = \ln \sigma_u^* - d_\sigma \ln b \quad (3)$$

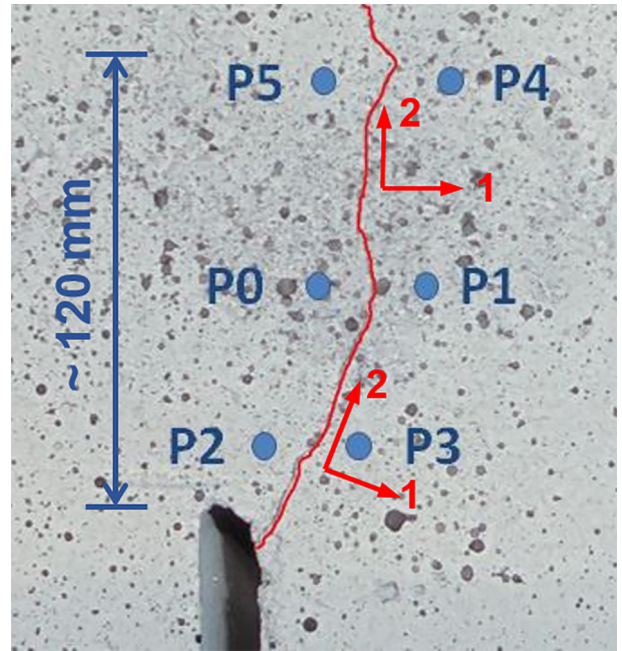


Fig. 7. Points near the crack at notch tip analysed by DIC. The crack path is highlighted in red. (For interpretation of the references to colour in this figure legend, the reader is referred to the web version of this article.)

with  $d_\sigma = 0.36$ ,  $\sigma_u^* = 22.6 \text{ Nmm}^{-1.64}$  (fractal dimension  $\Delta_\sigma = 2 - d_\sigma = 1.64$ ).

Fig. 3b shows fracture energy vs. beam depth for each test. The corresponding fractal scaling law is:

$$\ln G_F = \ln G_F^* + d_G \ln b \quad (4)$$

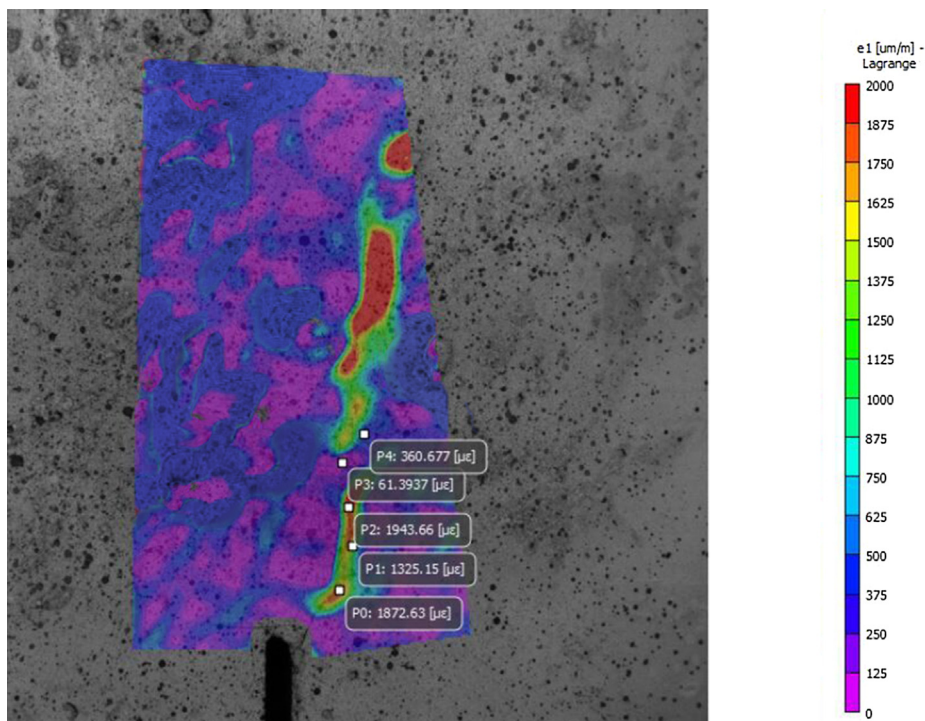


Fig. 6. Contour plot and point values of principal tensile strain  $\epsilon_1$  obtained by DIC for a specimen with  $b = 400 \text{ mm}$  (P0: 1872.63  $\mu\epsilon$ , P1: 1325.15  $\mu\epsilon$ , P2: 1943.66  $\mu\epsilon$ , P3: 61.3937  $\mu\epsilon$ , P4: 360.677  $\mu\epsilon$ ).

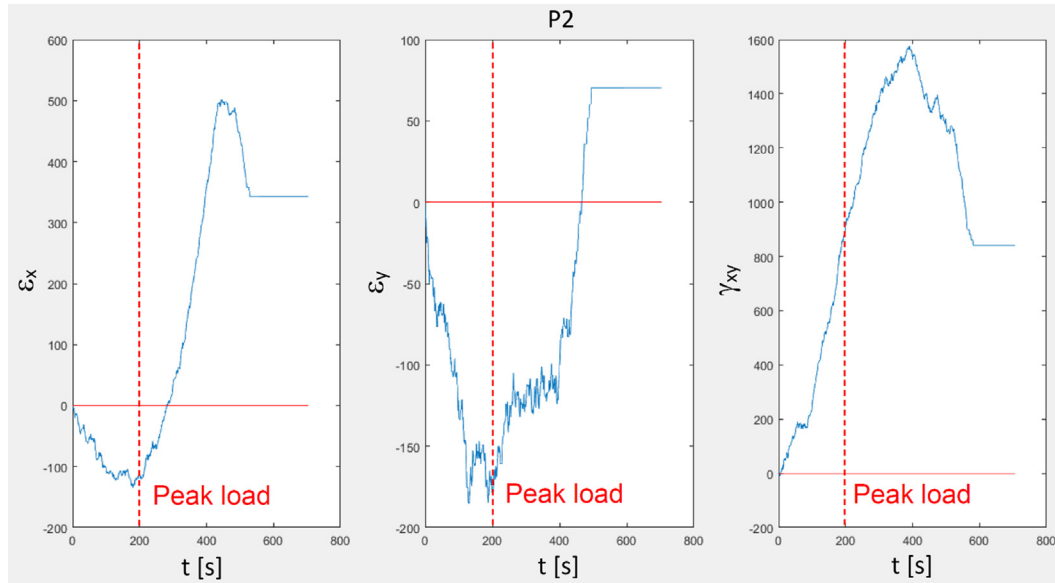


Fig. 8. Point P2: strain components  $\varepsilon_x$ ,  $\varepsilon_y$ ,  $\gamma_{xy}$  (in  $10^{-6}$ ).

with  $d_G = 0.19$ ,  $G_F^* = 209.9 \text{ Jm}^{-2.19}$  (fractal dimension  $\Delta_G = 2 + d_G = 2.19$ ).

Moreover, it is possible to define the critical value of the localized rotation for each TPB test [29]: these values are graphically represented in the bi-logarithmic diagram of Fig. 3c. As a matter of fact, at beam failure the rotation angle can be evaluated as  $\varphi_c = \frac{\delta_c}{L/2}$ , where  $\delta_c$  represent the beam mid-span deflection. Hence, the renormalized critical rotation,  $\varphi_c^*$ , arising from the power-law  $\varphi_c = \varphi_c^* b^{-d_\chi}$ , results to be intermediate between a dimensionless rotation angle and a radius of curvature [29]. Since a rotation angle is dimensionless, a radius of curvature has dimension  $[L]^1$ , whereas a curvature has dimension  $[L]^{-1}$ , the inverse of the renormalized critical rotation returns the renormalized critical curvature,  $\chi_c^*$ . From Fig. 3c, the relevant fractal scaling law provides:  $d_\chi = 0.49$ , and  $\chi_c^* = 33.45 \text{ mm}^{-0.49}$ .

In Fig. 4, the load and cumulative AE vs. time diagrams of three tests, i.e.  $b = 100$ ;  $300$ ;  $400$  mm, are shown. It is interesting to remark how the increase in beam size leads to an increase in brittleness, as shown by the post-peak regime in the loading process: from a slight softening post-peak behaviour for  $b = 100$  mm, to a steeper post-peak branch for  $b = 400$  mm [10]. The size-scale transition from ductile to brittle behaviour is governed by a non-dimensional Brittleness Number  $s_E$  [10,30], which is function of material properties and structural size-scale:  $s_E = \frac{G_F}{\sigma_u b}$ . As a matter of fact, we move from  $s_E = 2.9 \cdot 10^{-4}$  for the more ductile specimen with  $b = 100$  mm, to  $s_E = 1.7 \cdot 10^{-4}$  for the more brittle specimen with  $b = 400$  mm.

Concerning AE activity, its behaviour is in strict dependence to the damaging process in brittle materials [7,10,31–33]: this process occurs with an increase in strain coupled with global or local drops in the load carrying capacity, and the resulting emitted energy appears with an increase in the AE cumulative curve. Also for a globally smooth loading branch, small snap-back instabilities hidden in the loading process [7,10] cause a smooth AE cumulated curve (Fig. 4).

Fig. 5 shows the AE energy per unit area vs. beam depth for  $b = 100$ ;  $300$ ;  $400$  mm. The fractal scaling law is:

$$\ln \bar{E}_{AE} = \ln \bar{E}_{AE}^* - d_{AE} \ln b \quad (5)$$

with  $d_{AE} = 0.26$ ,  $\bar{E}_{AE}^* = 17,800 \text{ msVm}^{-1.74}$  (fractal dimension  $\Delta_{AE} = 2 - d_{AE} = 1.74$ ).

Unlike fracture energy, that is dissipated in an invasive fractal domain, AE energy detected during TPB tests turns out to be emitted in a lacunar fractal domain. This difference in the fractal physical dimensions indicates the un-correlation between dissipated and emitted energies: the total energy released during the test is equal to the sum of two un-correlated phenomena: the dissipated energy, representing a material property that is fracture energy,  $G_F$ , and the emitted energy during the snap-back phenomena, characterising AE energy [7–10].

The time evolution of strains around the notch was obtained by DIC measurements. Fig. 6 shows the contour plot and values of principal tensile strain,  $\varepsilon_1$ , at five points (P0–P4) along the crack, close to the notch, for a test made on a beam with  $b = 400$  mm.

For each point in the region of analysis, the DIC technique allows us to evaluate the variation of the surface strain state during the test; as is well-known, it can be represented by the strain tensor [34]:

$$[\varepsilon] = \begin{bmatrix} \varepsilon_x & \varepsilon_{xy} \\ \varepsilon_{yx} & \varepsilon_y \end{bmatrix} \quad (6)$$

where  $\varepsilon_{xy} = \varepsilon_{yx} = \frac{1}{2} \gamma_{xy}$  ( $x$ ,  $y$  representing the horizontal, vertical direction).

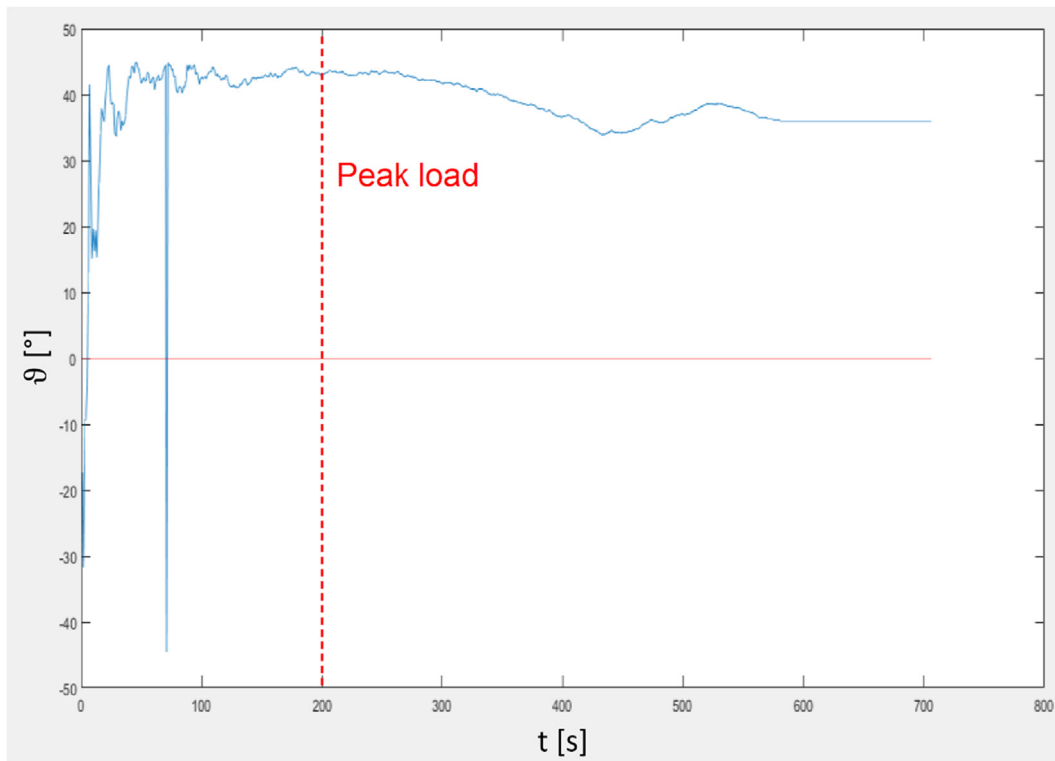
Therefore, principal strains and their directions during the test can be evaluated through the calculation of the eigenvalues and eigenvectors of the strain tensor, or, equivalently, by the following relationships based on Mohr's circle [34]:

$$\varepsilon_{1,2} = \frac{\varepsilon_x + \varepsilon_y}{2} \pm \frac{1}{2} \sqrt{(\varepsilon_x - \varepsilon_y)^2 + \gamma_{xy}^2},$$

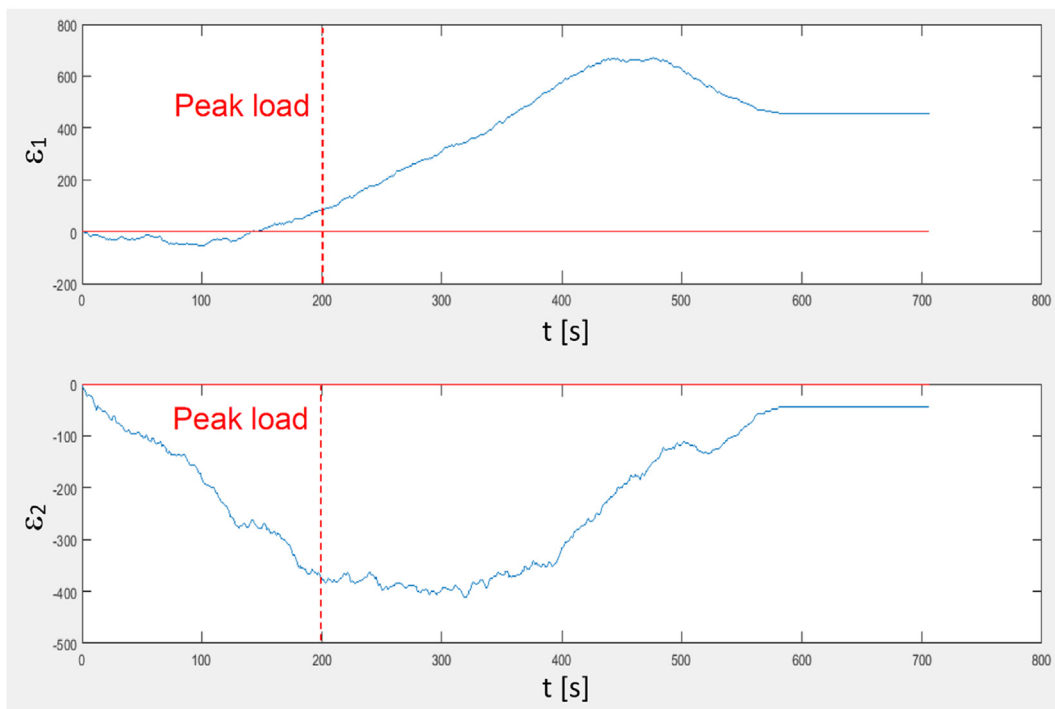
$$\vartheta = \frac{1}{2} \arctan \left( \frac{\gamma_{xy}}{\varepsilon_x - \varepsilon_y} \right) \quad \text{with} \quad -\frac{\pi}{4} < \vartheta < \frac{\pi}{4} \quad (7a, b)$$

where positive, negative strain means elongation, contraction, and the angle  $\vartheta$  (between directions  $x$  and  $1$ ) is positive if clockwise.

Fig. 7 shows six points, three on the left and three on the right of the crack originated at the notch tip, analysed by DIC. The crack path, highlighted in red, can be approximately described by an inclined line segment between the notch tip and points P0, P1



(a)



(b)

**Fig. 9.** Point P2: (a) angle of the principal strain direction system,  $\vartheta$ ; (b) principal strains,  $\varepsilon_1$ ,  $\varepsilon_2$  (in  $10^{-6}$ ).

(far about 60 mm on the vertical from the notch tip), and a vertical line segment between points P0, P1 and P4, P5 (far about 120 mm on the vertical from the notch tip). In Figs. 8–13, results for strains and angle and  $\vartheta$  are shown for points P2, P5, and P4; The peak load

was reached around 200 s since the beginning of the test (see also Fig. 4c), and is marked by a vertical dashed line in Figs. 8–13. From Fig. 8, we see that, near the notch tip, the horizontal strain,  $\varepsilon_x$ , is (mainly) an elongation, and the vertical one,  $\varepsilon_y$ , is a contraction.

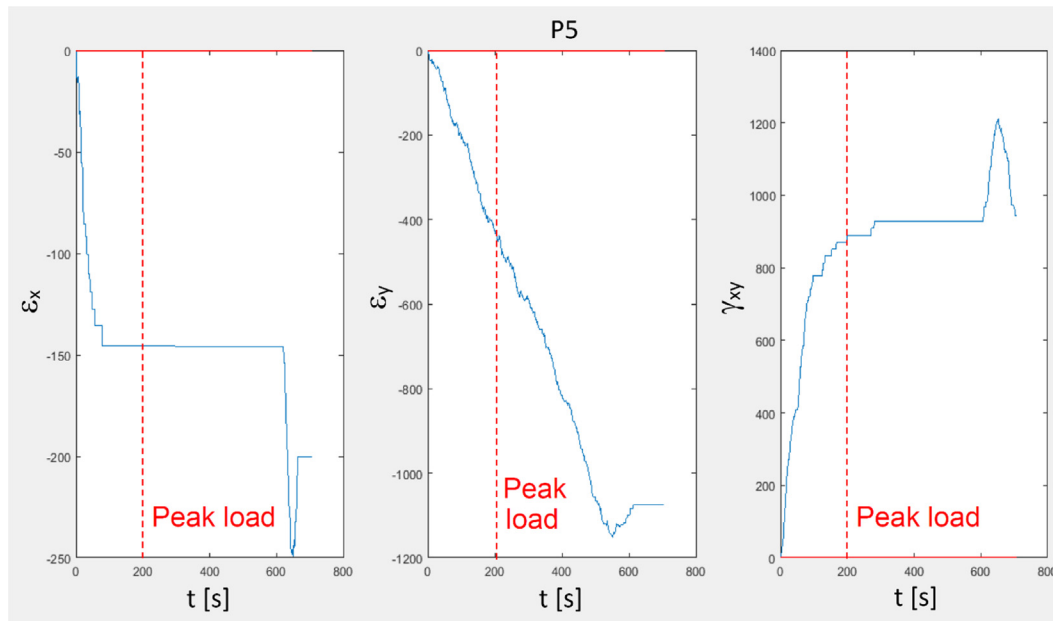


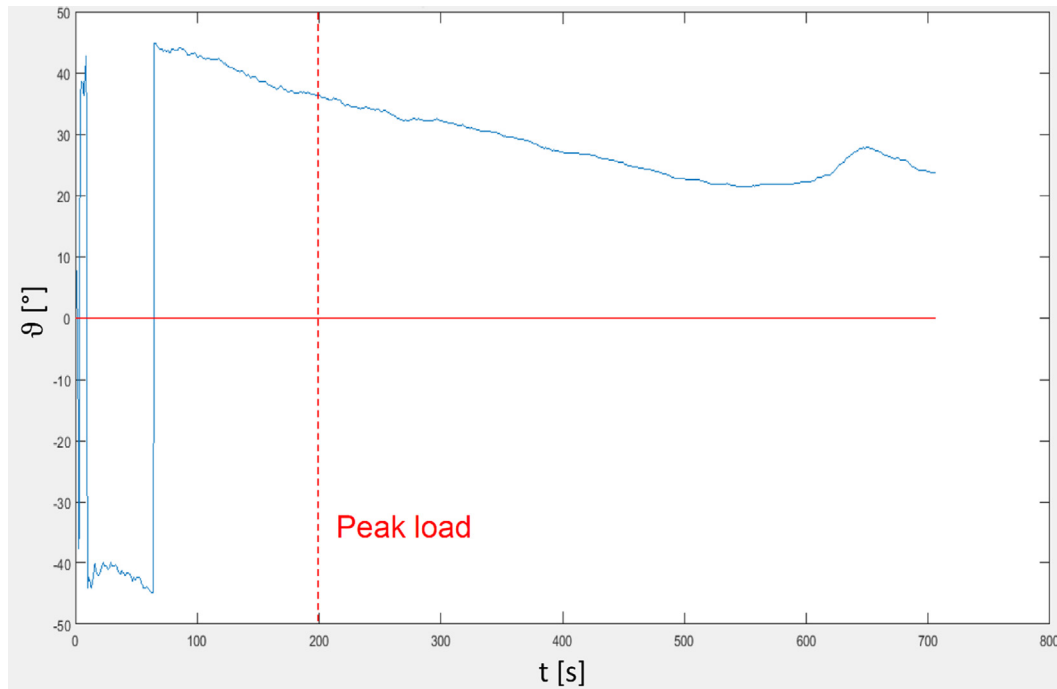
Fig. 10. Point P5: strain components  $\varepsilon_x$ ,  $\varepsilon_y$ ,  $\gamma_{xy}$ .

Also, from Fig. 9a, we see that the principal strain direction system at point P2 is rotated by  $40^\circ$  approximately with respect to the horizontal axis,  $x$ ; that almost for the entire test. Principal strains  $\varepsilon_1$ ,  $\varepsilon_2$  at point P2 are shown in Fig. 9b. In Fig. 8, vertical drops in  $\varepsilon_x$ ,  $\gamma_{xy}$  strains after the peak load (i.e. around 450 s), indicate that the crack has propagated up to that depth from the notch tip (stress release). Moving away from the notch tip, the crack path tends to straighten up, as it is shown in Fig. 7. From Figs. 10 and 12, we see that at points P4 and P5 horizontal and vertical strains,  $\varepsilon_x$  and  $\varepsilon_y$ , are both contractions. Moreover, they indicate that the crack has propagated up to that level after about 650 s from the beginning of the test. From Figs. 11a and 13a we see that the angle of the principal strain direction system diminishes from about  $45^\circ$  of the initial stages to about  $25^\circ$  and  $10^\circ$  of the final stages, for points P5 and P4, respectively. The corresponding principal strains are shown in Figs. 11b and 13b. We note that the strain/stress state in the mid-span region produced by the loading, is perturbed both by the presence of the initial notch and the effect of the advancing crack.

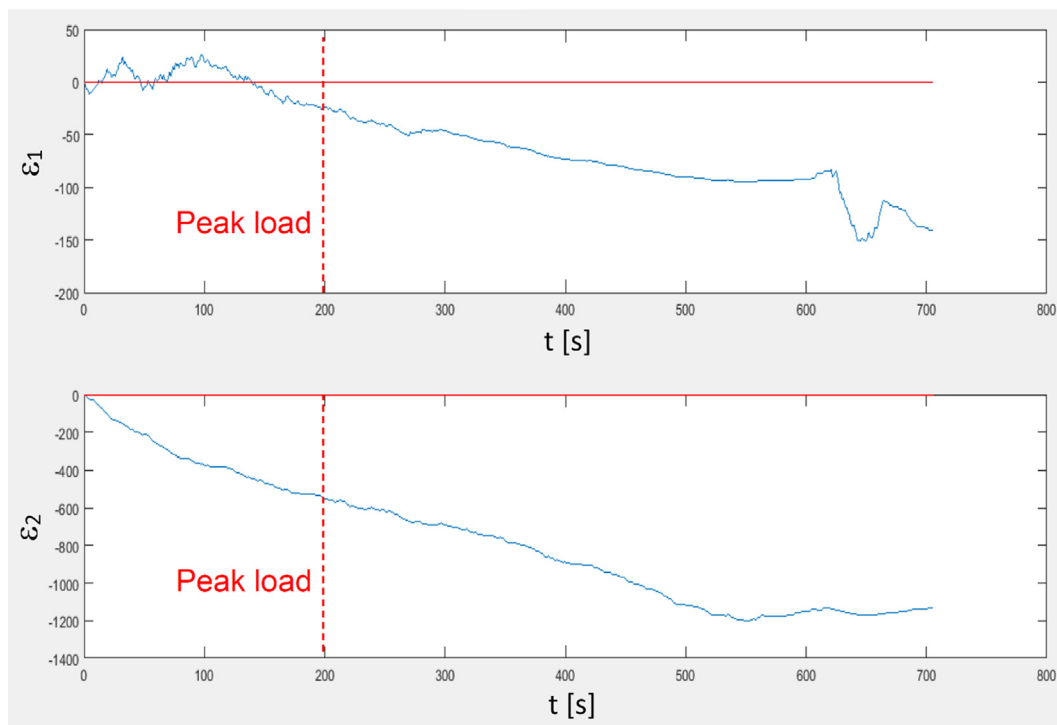
Analysis of AE indicators such as the average frequency (AF) and RA can give information on the crack propagation mode, i.e. mode I (opening) vs. mode II (sliding). For each AE signal, the two previous indices can be computed from wave parameters as: Average frequency = Counts/Duration, RA = Rise time/Maximum amplitude. Counts are the number of amplitude threshold crossings; Duration is the time between first and last signal amplitude above the threshold level; Rise time is the time between the first threshold crossing and the time corresponding to the maximum signal amplitude. Tensile cracks (mode I) are characterised by relatively high AF and low RA values (P-waves). Conversely, shear cracks (mode II) are characterised by relatively low AF and high RA values (S-waves) [35–37]. In Fig. 14a, the load vs. time and RA vs. time (for each AE event) for TPB test on a beam with  $b = 400$  mm (the same of Fig. 4c). Fig. 14b shows the AF vs. Ra values for the same test: we see that most of the values lie to the left of the diagonal line, thus indicating a dominant presence of tensile cracks; however, signals related to shear cracks were also detected. In particular, AE data in Fig. 14a show a first phase with mode I propagation

(points below the dashed line), a second phase with both mode I and mode II (points above the dashed line) cracks, and a third and last phase again characterised by mode I signals. These results are consistent with both the crack path in Fig. 7 and DIC data in Figs. 8–13.

In Fig. 15a, the load and the first three vertical bending frequencies are plotted vs. the mid-span deflection for a TPB test made on a beam with  $b = 400$  mm. Notice that eleven values are reported for each modal frequency in correspondence to as many loading steps, identified by the vertical loading reductions. The load losses are due to stopping the test (which was conducted in a displacement-controlled mode) for exciting the beam by impulsive forces, transmitted by a non-instrumented hammer; however, as it can be seen in the figure, each loading loss was always automatically recovered when the test restarted, so the curve is globally regular. Output only technique was used for identifying the resonant frequencies (excitations signals were not registered). Each frequency value is the mean of nine records, i.e., three reads for each pickup sensor. Standard deviations are very small (see error bars in the graph), thus indicating a low dispersion of data. As it is known, the natural frequencies decrease with damage, i.e., as the beam stiffness decreases with crack advancement: as it will be shown later on, this could be used to estimate the crack depth by means of numerical models, starting from measured frequency values [23,24]. The first, second, and third frequency at the beginning of the test (initial notch depth), are respectively equal to: 693, 815, and 2102 Hz. Their values remain constant up to the peak load, after which they start decreasing for the entire softening branch down to the final collapse. The percentage reductions of the frequencies with respect to their initial value, reported in the graph, are equal to 5.8%, 5.7%, and 12.7% for the first, second, and third natural frequency, respectively. Extrapolation could be used to obtain predictions for the final loading stages, where frequencies were not extracted to avoid the risk of breaking the specimen by the external excitation. Fig. 15b shows the mode shapes corresponding to the frequencies in Fig. 15a at the beginning of the test (i.e., for the initial notch depth), obtained by a 2-D finite element model implemented in LUSAS software [38]: mode 1 is symmetric with a node at mid-length, mode 2 is antisymmetric with a node at



(a)



(b)

Fig. 11. Point P5: (a) angle of the principal strain direction system,  $\vartheta$ ; (b) principal strains,  $\epsilon_1$ ,  $\epsilon_2$  (in  $10^{-6}$ ).

the mid-length, mode 3 is antisymmetric with three nodes. Notice that all mode shapes present a node in correspondence to the central support (loading point), where there is the notch.

Four-node quadrilateral plane stress elements (QPM4) were used to model the beam. Properties for linear elastic material were set as follows: Young's modulus  $E = 30,570$  MPa; Poisson's

ratio = 0.15; mass density  $\rho = 2310$  kg/m<sup>3</sup>. The beam was constrained by preventing the vertical displacements in correspondence to the end and intermediate sections. Free vibration analyses were run for increasing values of the relative notch depth  $a/b$ , from 0.5 (initial value) to 0.95, with increments of 0.05. The analyses were all run with respect to the undeformed configura-

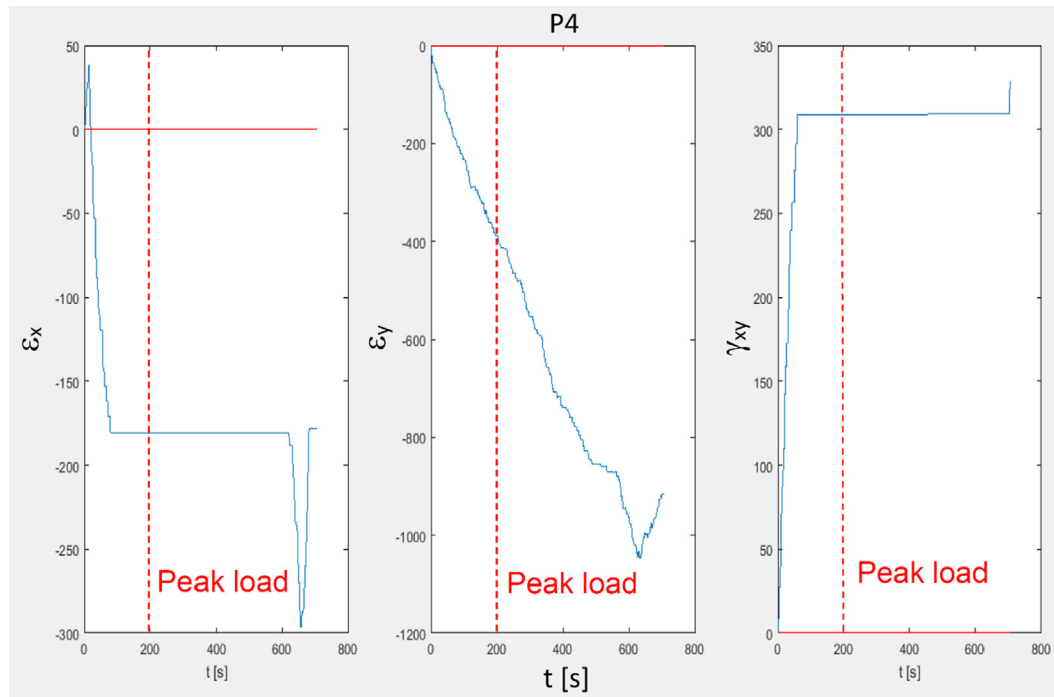


Fig. 12. Point P4: strain components  $\epsilon_x$ ,  $\epsilon_y$ ,  $\gamma_{xy}$ .

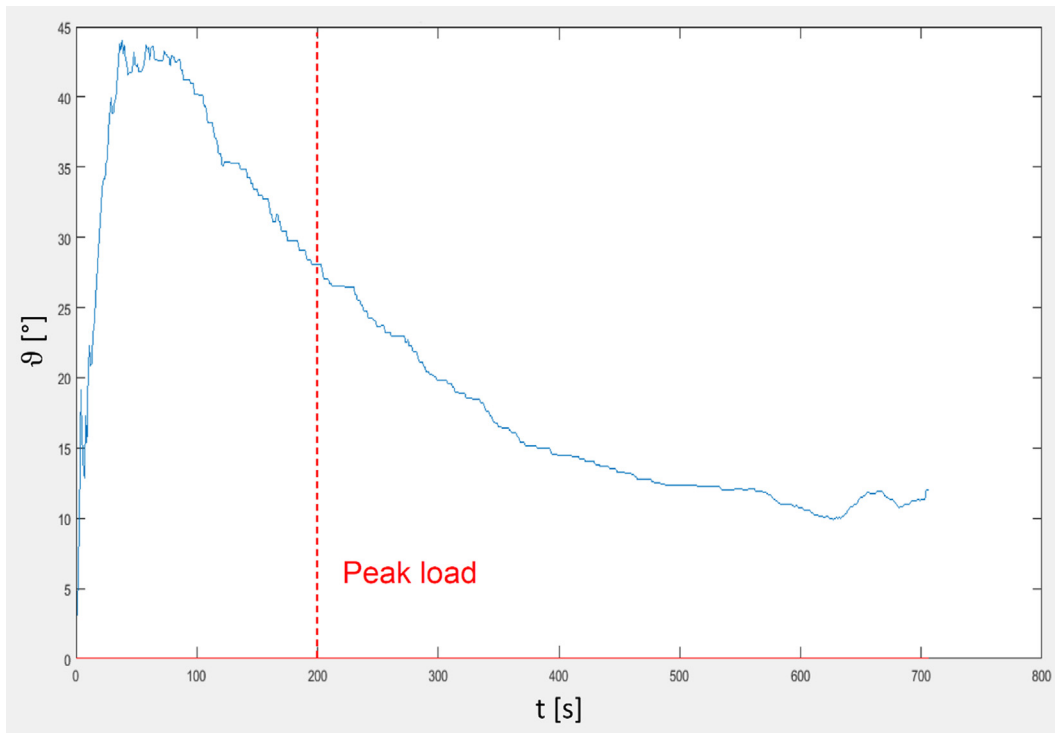
tion, in stress-free conditions (geometric nonlinearity is negligible). The first three numerical frequencies, for the initial notch depth, are respectively equal to: 742, 774, and 2053 Hz. They differ from the corresponding experimental ones by 7.0,  $-5.0$ , and  $-2.3$  per cent, respectively. Fig. 15c shows their variations vs. the relative notch depth, represented by a monotonic decrease with the ratio  $a/b$ . By comparing the measured frequency reductions and the calculated ones in Fig. 15c, one can get a rapid, approximate estimate of the crack depth. For example, for  $a/b = 0.65$ , the first three numerical frequencies result reduced by 9.0%, 3.6%, and 10.0%. We note that the FEM model presented here is rather simplified, and more accurate numerical predictions could be obtained by more refined models.

#### 4. Conclusions

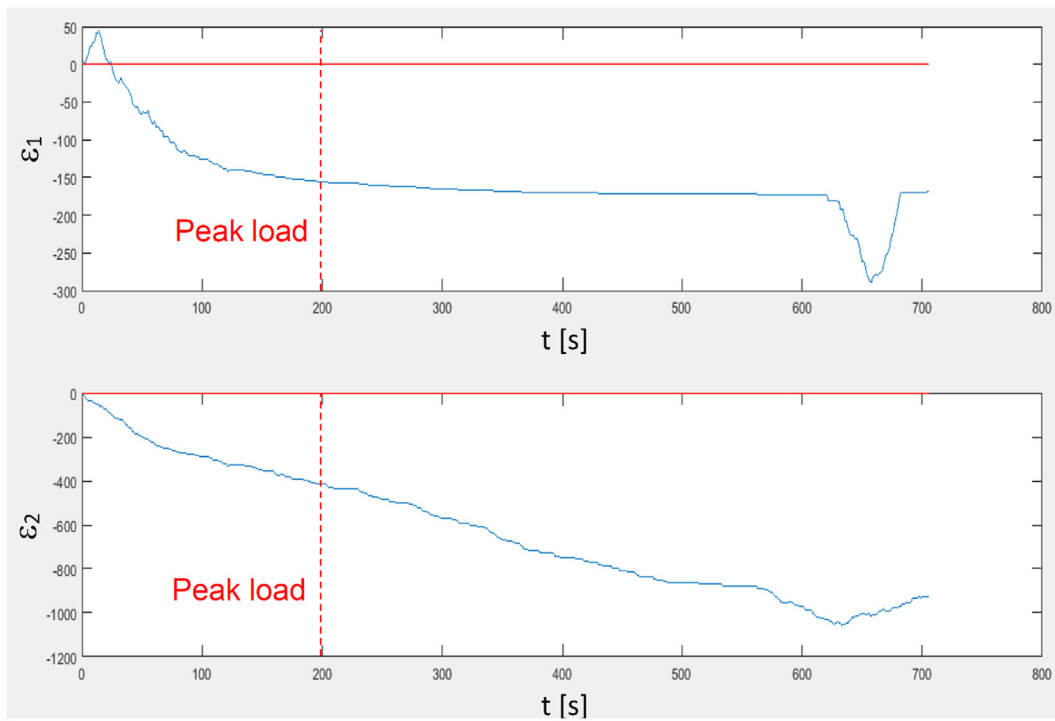
Three-point bending tests were performed on plain concrete pre-notched specimens of four different sizes. In the first part of the study, scale effects on fracture energy, bending strength and AE energy per unit area were investigated. The fractal model was applied to define scaling laws and renormalized scale-invariant values for the above-mentioned parameters. Beside confirming well known results such as fractal dimension of material ligament at peak stress is comprised between 1 and 2 (lacunar domain) and fractal dimension of fracture surface at failure is comprised between 2 and 3 (invasive domain), an new, interesting result was obtained for AE energy per unit area: the data furnished a fractal dimension of Acoustic Emission area comprised between 1 and 2. This indicates that fracture energy and AE energy have different origins: while the former is dissipated, to produce fracturing, on an invasive fractal domain, the latter results to be emitted, when damage occurs, on a lacunar fractal domain. Obviously, this result is related to the specimens analysed here, and further investigations on a larger number of specimens are suggested to wider the statistics.

In the second part of the study, engineering information of practical interest were obtained by combining DIC, AE and DI techniques. By the former, the strain state around the notch was evaluated and principal strains and their directions were obtained for points close to the main crack. Such information can be used for estimating the distance from a conventional cracking strain level for integer material, as well as to identify the crack advancement and its path after first cracking. For concrete, for example, strains corresponding to tensile fracturing are of order  $10^{-4}$  (around 0.1 or 0.2‰, the value depending on material tensile strength and elastic modulus). In general, the accuracy of DIC strain evaluation and crack detection depends on measuring points map, material's heterogeneity and elastic modulus, setting parameters, etc., as pointed out by some specific studies [39,40]. As regards AE signals, average frequency vs. RA value analysis was used to characterise the crack mode (tensile vs. shear) during the tests. Lastly, DI was used to correlate the decrease in resonant bending frequencies with the crack advancement by an inverse procedure. In particular, the crack depth at different loading levels was estimated by comparing the measured resonant frequencies with those given by finite element models of similar beams with increasing relative notch depths.

In principle, the multi-technique approach applied here to laboratory tests on small-size specimens can be extended to real world structures to realise a more effective and reliable monitoring. Investigation may proceed from global behaviour to local analysis, as well as by crossing the information from the different techniques. For example, modal frequencies, shapes and curvatures can be used to detect anomalies in the dynamic behaviour of a structure with respect to the undamaged state, and to detect the possible damaged regions. Thus, AE sensors and DIC apparatus can be placed around those specific regions and the relevant data, together with the dynamic parameters, used for monitoring the structural health or damage evolution process.



(a)



(b)

**Fig. 13.** Point P4: (a) angle of the principal strain direction system,  $\vartheta$ ; (b) principal strains,  $\epsilon_1$ ,  $\epsilon_2$  (in  $10^{-6}$ ).

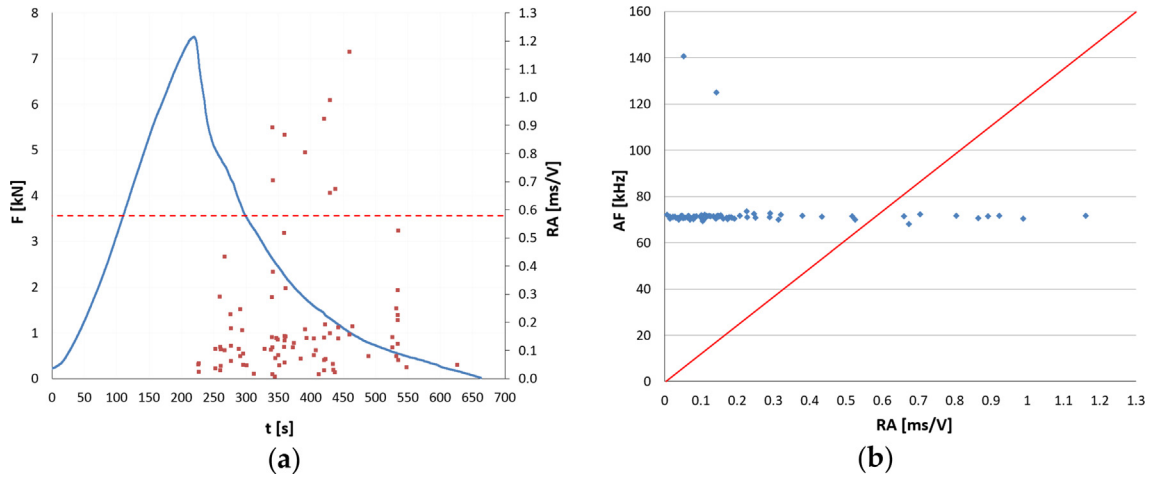


Fig. 14. (a) Load and RA vs. time, and (b) AF vs. RA for TPB test on a beam with  $b = 400$  mm (Fig. 4c).

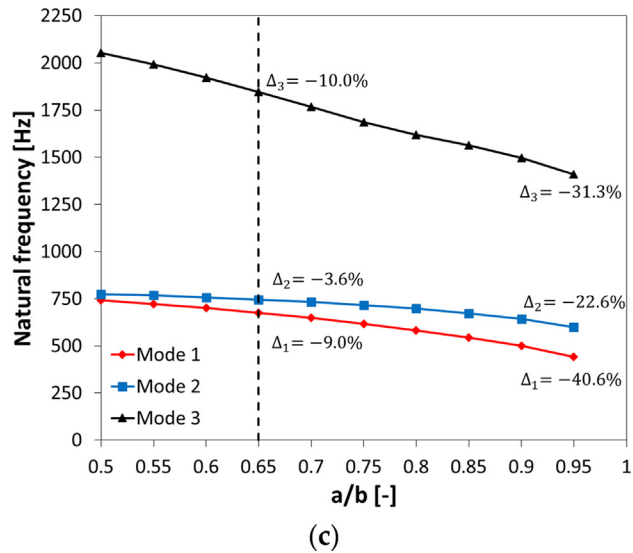
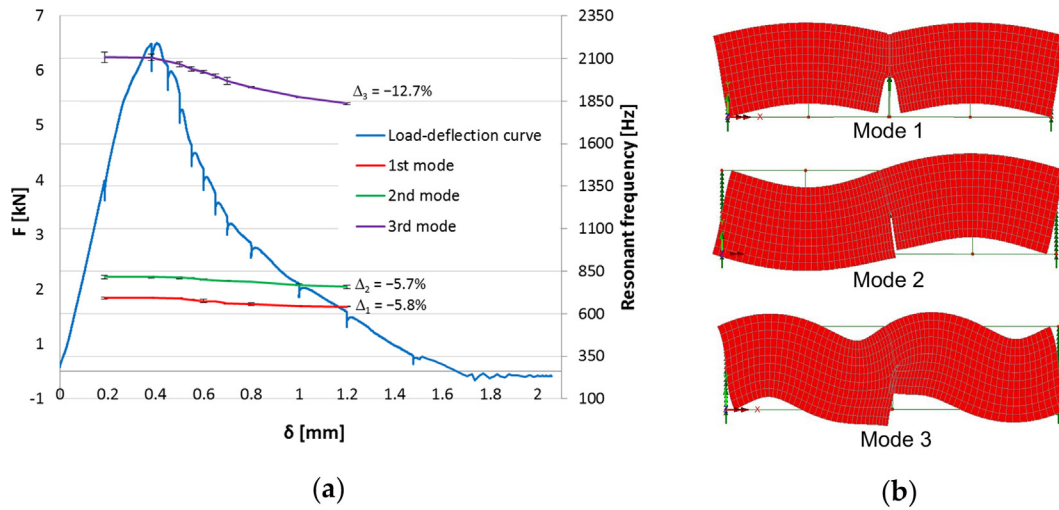


Fig. 15. (a) experimental load and resonant bending frequencies vs. displacement curves from TPB test made on a beam with  $b = 400$  mm; (b) corresponding mode shapes for initial notch depth from finite element analysis; (c) FEM natural bending frequencies vs. notch depth,  $a/b$ , for a beam with  $b = 400$  mm.

## CRedit authorship contribution statement

**Giuseppe Lacidogna:** Conceptualization. **Gianfranco Piana:** Investigation, Formal analysis. **Federico Accornero:** Investigation, Formal analysis. **Alberto Carpinteri:** Supervision.

## Declaration of Competing Interest

The authors declare that they have no known competing financial interests or personal relationships that could have appeared to influence the work reported in this paper.

## References

- [1] A. Carpinteri, Decrease of apparent tensile and bending strength with specimen size: Two different explanations based on fracture mechanics, *Int. J. Solids Struct.* 25 (1989) 407–429.
- [2] RILEM TC50-FMC Draft Recommendation, Determination of fracture energy of mortar and concrete by means of three-point bend tests on notched beams, *Mater. Struct.* 18 (1985) 285–290.
- [3] RILEM TC QFS Recommendation, Quasibrittle fracture scaling and size effect—Final report, *Mater. Struct.* 37 (2004) 547–568.
- [4] L.R. Botvina, The benefits and challenges of interdisciplinary research, *Phys. Mesomech.* 22 (2019) 5–12.
- [5] G. Lacidogna, F. Accornero, A. Carpinteri, Masonry structures. In: *Innovative AE and NDT Techniques for On-site Measurement of Concrete and Masonry Structures (RILEM)*; Ohtsu, M., Ed.; Chapter 3; Springer, Heidelberg, Germany, 2016; pp. 27–46. doi: 10.1007/978-94-017-7606-6\_3.
- [6] K. Ohno, M. Ohtsu, Crack classification in concrete based on acoustic emission, *Constr. Build. Mater.* 24 (2010) 2339–2346.
- [7] A. Carpinteri, F. Accornero, Multiple snap-back instabilities in progressive microcracking coalescence, *Eng. Fract. Mech.* 187 (2018) 272–281.
- [8] G. Lacidogna, F. Accornero, M. Corrado, A. Carpinteri, Crushing and fracture energies in concrete specimens monitored by Acoustic Emission, in: *Proceedings of the 8th International Conference on Fracture Mechanics of Concrete and Concrete Structures, FraMCoS 2013*, 2013, pp. 1726–1736.
- [9] A. Carpinteri, G. Lacidogna, G. Niccolini, S. Puzzi, Morphological fractal dimension versus power-law exponent in the scaling of damaged media, *Int. J. Damage Mech.* 18 (2009) 259–282.
- [10] G. Lacidogna, F. Accornero, A. Carpinteri, Influence of snap-back instabilities on Acoustic Emission damage monitoring, *Eng. Fract. Mech.* 210 (2019) 3–12.
- [11] M.A. Sutton, J.J. Ortu, H. Schreie, *Image Correlation for Shape, Motion and Deformation Measurements. Basic Concepts, Theory and Application*, Springer, New York, NY, USA, 2009.
- [12] D.G. Aggelis, S. Verbruggen, E. Tsangouri, T. Tysmans, D. van Hemelrijck, Characterization of mechanical performance of concrete beams with external reinforcement by acoustic emission and digital image correlation, *Constr. Build. Mater.* 47 (2013) 1037–1045.
- [13] K. Shrama, On the use of acoustic emission and digital image correlation for welded joints damage characterization, *J. Appl. Comput. Mech.* 5 (2) (2019) 381–389.
- [14] G. Livitsanos, N. Shetty, E. Verstryngge, M. Wevers, D. van Hemelrijck, D.G. Aggelis, Shear failure characterization in masonry components made with different mortars based on combined NDT methods, *Constr. Build. Mater.* 220 (2019) 690–700.
- [15] Ł. Skarżyński, J. Tejchman, Experimental investigations of fracture process using DIC in plain and reinforced concrete beams under bending, *Strain* 49 (6) (2013) 521–543.
- [16] G. Hearn, R.B. Testa, Modal analysis damage detection in structures, *J. Struct. Eng.* 117 (10) (1991) 3042–3063.
- [17] S. Hassiotis, G.D. Jeong, Assessment of structural damage from natural frequency measurements, *Comp. Struct.* 49 (4) (1993) 679–691.
- [18] A.K. Pandey, M. Biswas, M.M. Samman, Damage detection in structures using changes in flexibility, *J. Sound Vib.* 169 (1) (1994) 3–17.
- [19] J.R. Casas, A.C. Aparicio, Structural damage identification from dynamic-test data, *J. Struct. Eng.* 120 (8) (1994) 2437–2450.
- [20] S. Hassiotis, G.D. Jeong, Identification of stiffness reduction using natural frequencies, *J. Eng. Mech.* 121 (10) (1995) 1106–1113.
- [21] J.F. Doyle, Determining the size and location of transverse cracks in beams, *Exp. Mech.* 35 (3) (1995) 272–285.
- [22] D. Dessi, G. Camerlengo, Damage identification techniques via modal curvature analysis: overview and comparison, *Mech. Syst. Signal Process.* 52–53 (2015) 181–205.
- [23] G. Lacidogna, G. Piana, A. Carpinteri, Acoustic emission and modal frequency variation in concrete specimens under four-point bending, *Appl. Sci.* 7 (2017) 339, <https://doi.org/10.3390/app7040339>.
- [24] G. Lacidogna, G. Piana, A. Carpinteri, Damage monitoring of three-point bending concrete specimens by acoustic emission and resonant frequency analysis, *Eng. Fract. Mech.* 210 (2019) 203–211.
- [25] G. Piana, E. Lofrano, A. Carpinteri, A. Paolone, G. Ruta, Experimental modal analysis of straight and curved slender beams by piezoelectric transducers, *Meccanica* 51 (11) (2016) 2797–2811.
- [26] G.I. Barenblatt, *Flow, Deformation and Fracture*, Cambridge University Press, 2014.
- [27] G.I. Barenblatt, L.R. Botvina, A note concerning power-type constitutive equations of deformation and fracture of solids, *Int. J. Eng. Sci.* 20 (1982) 187–191.
- [28] R.V. Goldstein, A.B. Mosolov, Fractal cracks, *J. Appl. Math. Mech.* 56 (1992) 563–571.
- [29] A. Carpinteri, F. Accornero, Rotation versus curvature fractal scaling in bending failure, *Phys. Mesomech.* 22 (2019) 46–51.
- [30] K.G. Wilson, Renormalization group and critical phenomena, *Phys. Rev. B* 4 (1971) 3174–3183.
- [31] A. Carpinteri, G. Lacidogna, F. Accornero, A. Mpalaskas, T. Matikas, D. Aggelis, Influence of damage in the Acoustic Emission parameters, *Cem. Concr. Compos.* 44 (2013) 9–16.
- [32] A. Carpinteri, G. Lacidogna, F. Accornero, Fluctuations of 1/f noise in damaging structures analyzed by Acoustic Emission, *Appl. Sci.* 8 (2018) 1685.
- [33] L.R. Botvina, A.D. Zavyalov, Interdisciplinary problems of fracture physics and mechanics: from metals to rocks. II. Fracture criteria, *Russian Metall. (Metally)* 10 (2018) 893–903.
- [34] S.P. Timoshenko, J.N. Goodier, *Theory of Elasticity*. McGraw-Hill, Tokyo, 1970.
- [35] Recommendation of RILEM TC 212-ACD. Acoustic emission and related NDE techniques for crack detection and damage evaluation in concrete: Measurement method for acoustic emission signals in concrete. *Mater. Struct.* 43 (2010) 1177–1181.
- [36] Recommendation of RILEM TC 212-ACD. Acoustic emission and related NDE techniques for crack detection and damage evaluation in concrete: Test method for damage qualification of reinforced concrete beams by acoustic emission. *Mater. Struct.* 43 (2010) 1183–1186.
- [37] Recommendation of RILEM TC 212-ACD. Acoustic emission and related NDE techniques for crack detection and damage evaluation in concrete: Test method for classification of active cracks in concrete by acoustic emission. *Mater. Struct.* 43 (2010) 1187–1189.
- [38] LUSAS. User Reference Manual (version 15.1), FEA Ltd., Kingston upon Thames, Surrey, UK, 2015.
- [39] I. Khelifi, J.C. Dupré, P. Doumalin, Y. Belrhiti, O. Pop, M. Huger, Improvement of Digital Image Correlation for the analysis of the fracture behaviour of Refractories. 23ème Congrès Français de Mécanique. Lille, 28 Août au 1er Septembre 2017.
- [40] M. Bornert et al., Assessment of digital image correlation measurement errors: methodology and results, *Exp. Mech.* 49 (2009) 353–370.